Proceedings of the ECCOMAS Thematic International Conference on Simulation and Modeling of Biological Flows (SIMBIO 2011)
September 21–23, 2011, VUB, Brussels, Belgium

Investigations of the Inspiration and Heating Capability of the Human Nasal Cavity Based on a Lattice-Boltzmann Method

Andreas Lintermann, Matthias Meinke, Wolfgang Schröder

Institute of Aerodynamics and Chair of Fluid Mechanics, RWTH Aachen University
Wüllnerstr. 5a, 52062, Aachen, Germany, A.Lintermann@aia.rwth-aachen.de

Abstract

Complaints like impaired respiration capabilities or a reduced sense of smell and taste are common for pathologically shaped nasal cavities. The *Lattice-Boltzmann Method (LBM)*, which is particularly suited to simulate flows in intricate geometries, is used to analyze the influence of the geometry of the nasal cavity on the pressure loss in a non-invasive pre-surgical step to support surgical decision processes. Another important function of the nasal cavity is the moisturization and heating of the inhaled air. To analyze complaints caused by a diminished heating function a passive scalar convection-diffusion equation for the temperature is solved by a *Thermal Lattice-Boltzmann Method*. After a successful validation of the method for the flow over a heated isothermal flat plate, a comparison of the functionalities of a modified nasal cavity after rhino-anaplasty and a cavity with swollen turbinates is performed to understand the influence of the geometry on the breathing capability and the ability to heat up the inhaled air.
Keywords: Lattice-Boltzmann, Thermal Lattice-Boltzmann, LBGK, TLBGK, Nasal cavity flows, Heated boundary-layer flows

Introduction

Rhinologists are often confronted with pathological shaped human nasal cavities. Impaired respiratory efficacy caused by allergies, mal- or deformations is only one aspect rhinologists need to consider in this case. A reduced sense of smell due to misled flows results not only in a diminished olfactory functionality, but also in a reduction of degustation. In addition, the nasal cavity plays an important role in the protection of the human lung. It is responsible for filtering out particles and aerosols from the inhaled air. Furthermore, the large surface of the human nasal cavity allows the moisturization and heating of the air to attain optimal conditions for the lower airways. These functions can be impaired by e.g., congenital malformations or rhino-anaplasty.

To analyze the functions of the cavity and to prevent deformations that affect these functions negatively, pre-surgical intervention planning by surgeons is based on *Computer Tomography (CT)* images and expert knowledge. The analysis of CT-images only accounts for the shape of the cavity and not for the functions determined by the flow field in the nasal cavity. The complexity of the geometry makes an understanding of these aspects difficult. The demand for a fundamental comprehension of the flow behavior has led to the application of numerical flow simulations to evaluate the impact of surgical interventions on these functions. This analysis supports the decision process and finally leads to *Computer Assisted Surgery (CAS)* [1].

The growth of computational power in recent years has increasingly replaced studies investigating the flow in silicon models of the nasal cavity with *Particle Image Velocimetry (PIV)* [2–5] by numerical simulations of flows on computer systems. Numerical investigations with a *Finite Volume (FV)* approach based on an AUSM-based discretization model of second-order accuracy on a multi-block structured grid were performed by Hörschler et al. in [6–8]. In a recent publication, Hörschler et al. state that for pulsatile flows in nasal cavities unsteady effects appear upon reaching the transition phase between in- and exhalation [9]. However, during the in- and exhalation phase, unsteady effects due to the changing mass flux are negligible so that steady inflow conditions at the maximum flow rate are used for the simulations in this paper for the determination of the pressure loss and the temperature field during inhalation.

The solutions for the nasal cavity are based on a *Lattice-Boltzmann Method (LBM)*. Due to the simplicity of the algorithm, the computation is performed very efficiently and has proven to be suited for bio-mechanical problems in the low MACH number and low REYNOLDS number regime [10, 11]. Finck et al. already simulated the flow in a model of the nasal cavity with the LBM [12]. Eitel et al. applies the same solution method but uses a geometry extracted from CT data [13]. An analysis of the heating capability is in both publications neglected. Since the LBM is not able to consider thermal impacts, this paper

uses a *Thermal Lattice-Boltzmann Method (TLBM)* to additionally solve for the temperature distribution. In general, there exist two approaches to include thermal effects. The *multi-speed (MS)* approach [14–16] extends the LBM by introducing new discrete velocities and equilibrium distribution functions with higher-order terms to represent the energy equation. The method used in this paper is the *multi-distribution (MD)* approach, which does not suffer from instabilities like the MS approach and is applicable to a wide temperature range [17, 18].

This article is organized as follows. First, an introduction to the numerical methods is given. In this context, the Lattice-Boltzmann and Thermal Lattice-Boltzmann Method to obtain the macroscopic variables, the automatic *Cartesian grid* generator to create the computational mesh, and the applied boundary conditions are described. To validate the simulation method, results of a boundary-layer problem of a flow over an isothermal flat plate are presented. Then, the flow in a nasal cavity modified in a rhino-anaplasty is investigated and a comparison to a nasal cavity with swollen turbinates is performed to understand the influence of the geometry on the breathing capability and the ability to heat the inhaled air to protect the lower airways. Finally, some conclusions are drawn along with a brief outlook.

Numerical Methods

Lattice-Boltzmann Method with Thermal Extension

The Lattice-Boltzmann Method is a gas-kinetic stochastical approach for the simulation of continuum flows and is based on solving the *Boltzmann equation* numerically. This equation describes the evolution of the number of molecules in a small but finite volume over time and consists of a collision and a transport term. The collision term specifies the win and loss of molecules due to collisions inside and outside the volume, while the transport term describes the temporal change, the convection and the influence of external forces. Bhatnagar, Gross and Krook expressed the collision term by a relaxation towards a thermodynamical equilibrium and yield the so-called *BGK-equation* [19], from which the *Navier-Stokes equations* can be recovered [20]. The discretization of this equation, under omittance of the forcing term, leads to

$$f_i\left(\vec{x}+\xi_i\delta t, t+\delta t\right) = f_i\left(\vec{x},t\right) + \omega\delta t\cdot\left(f_i^{eq}\left(\vec{x},t\right)-f_i\left(\vec{x},t\right)\right). \quad (1)$$

The relaxation towards the equilibrium, specified by the discretized *Maxwellian distribution function*

$$f^{eq}\left(x_\alpha,t\right)=\rho t_p\left[1+\frac{v_\alpha\xi_\alpha}{c_s^2}+\frac{v_\alpha v_\beta}{2c_s^2}\left(\frac{\xi_\alpha\xi_\beta}{c_s^2}-\delta_{\alpha\beta}\right)\right], \quad (2)$$

is given by the molecular collision frequency

$$\Omega=\omega\delta t=\frac{c_s^2\delta t}{\nu+1/2c_s^2\delta t}, \quad (3)$$

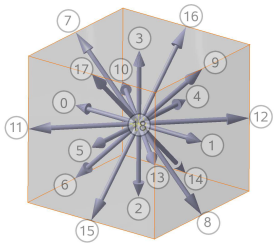

$$\xi_i=\xi_0\begin{cases}(\mp1,0,0)\,;(0,\mp1,0)\,;(0,0,\mp1) & \alpha=0\ldots5\\ (\mp1,\mp1,0)\,;(\mp1,0,\mp1)\,;(0,\mp1,\mp1) & \alpha=6\ldots17\\ (0,0,0) & \alpha=18\end{cases}$$

Figure 1 D3Q19 model for phase space discretization. In three dimensions 19 directions are specified to model molecular collision and propagation processes.

depending on the viscosity ν. In these equations $c_s=(1/\sqrt{3})(\delta x/\delta t)$ represents the speed of sound based on the grid distance δx and the time step δt, $v_{\alpha,\beta}$ the local velocities, $\delta_{\alpha,\beta}$ the *Kronecker delta* with $\alpha,\beta\in\{1,2,3\}$ and ρ the density. The molecular velocities are given by the variables ξ_i. The space is discretized with the D3Q19 model shown in Fig. 1, where the notation of DnQm was introduced by Quian et al. in [20] for specifying a dimensionality of n and a number of discrete directions and velocities of m. The parameters n and m also determine the weighting factors t_p. Eq. 1 is then solved for f_i, the so-called *particle probability distribution functions (PPDFs)*, which describe the probability to find a certain particle in phase space. This is done in two steps

$$f_i^{coll} \leftarrow f_i\left(\vec{x},t\right)+\Omega\cdot\left(f_i^{eq}\left(\vec{x},t\right)-f_i\left(\vec{x},t\right)\right) \quad (4)$$

$$f_i^{coll} \rightarrow f_i\left(\vec{x}+\xi_i\delta t, t+\delta t\right)^{prop}, \quad (5)$$

where a collision is performed locally in every cell (Eq. 4) and a streaming process propagates the information to the neighboring cells (Eq. 5). The density ρ and velocity v are obtained by evaluating the moments of the PPDFs as listed in Tab. 1. This method is called the *Lattice-BGK (LBGK)* method.

The BGK-approach is a quasi-incompressible method and is therefore only valid for MACH numbers $Ma\ll1$. A low MACH number expansion shows that the energy conservation equation decouples from the continuity and momentum conservation equation [21]. In this case, the pressure and the velocities become independent of the temperature and the energy is split into mechanical and thermal energy. To determine the temperature field, a transport equation for the thermal energy

$$\frac{\partial\rho c_pT}{\partial t}+\frac{\rho v_\alpha c_pT}{\partial x_\alpha}=\frac{\partial}{\partial x_\alpha}\left(\rho\kappa\frac{\partial T}{\partial x_\alpha}\right),\alpha\in\{1,2,3\} \quad (6)$$

is considered. In this equation c_p is the specific heat capacity, which is under the assumption of quasi-incompressibility together with ρ a constant. A division

Table 1 Derivation of macroscopic variables from moments of the PPDFs.

macr. variable	*discrete moment*
density	$\rho = \sum_{i=0}^{18} f_i = \sum_{i=0}^{18} f_i^{eq}$
momentum	$\rho v_\alpha = \sum_{i=0}^{18} \xi_{i,\alpha} f_i = \sum_{i=0}^{18} \xi_{i,\alpha} f_i^{eq}$
temperature	$T = \sum_{i=0}^{18} g_i = \sum_{i=0}^{18} g_i^{eq}$

by these variables yields

$$\frac{\partial T}{\partial t} + (\vec{v}\nabla_r)\, T = \kappa \nabla_r^2 T, \tag{7}$$

where κ is the heat conduction coefficient and can be expressed by the viscosity ν and the PRANDTL number Pr

$$\kappa = \frac{\nu}{Pr}. \tag{8}$$

The discretization of Eq. 7 leads to an equation similar to Eq. 1

$$\begin{aligned} g_i\left(\vec{x} + \xi_i \delta t, t + \delta t\right) \quad &= \quad g_i\left(\vec{x}, t\right) \\ &+ \Omega_T \cdot \left(g_i^{eq}\left(\vec{x}, t\right) - g_i\left(\vec{x}, t\right)\right), \end{aligned} \tag{9}$$

which is solved with an additional set of PPDFs g_i [22]. For an increasing κ, the collision frequency

$$\Omega_T = \frac{c_s^2 \delta t}{\kappa + 1/2 c_s^2 \delta t} \tag{10}$$

decreases. The equilibrium distribution functions g_i^{eq} are given by

$$g^{eq}\left(x_\alpha, t\right) = T t_p \left[1 + \frac{v_\alpha \xi_\alpha}{c_s^2} + \frac{v_\alpha v_\beta}{2 c_s^2}\left(\frac{\xi_\alpha \xi_\beta}{c_s^2} - \delta_{\alpha\beta}\right)\right], \tag{11}$$

where the velocities v_i come from the previously calculated LBGK-solution step. The temperature is then obtained from the zeroth moment of g_i (see Tab. 1). This solution method is called the *Thermal Lattice-BGK (TLBGK)* method.

The overall computational effort can be reduced by using the concept of grid refinement presented by Filippova et al. [23] and which was later extended by Dupuis et al. [24]. This method also allows to highly resolve wall-bounded shear layers, while regions of low macroscopic gradients have a lower resolution saving an unnecessary high number of cells. By using an overlay of fine and coarse cells at the interface region, information between different cell levels can be exchanged. On both levels in the interface region not all information is available and the macroscopic variables and the incoming PPDFs partially need to be reconstructed. This is also depicted in Fig. 2,

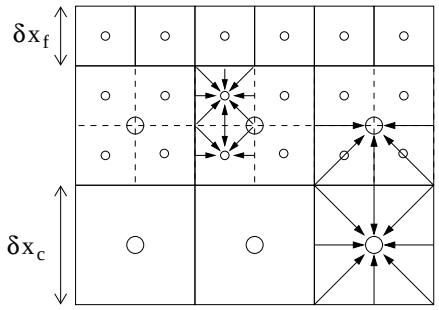

(a) Missing information at level interfaces, which need to be reconstructed.

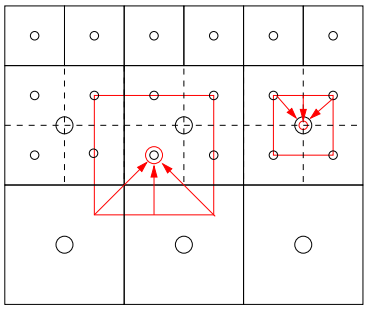

(b) Reconstruction of information by interpolation and transformation.

Figure 2 Refinement algorithm at interfaces between coarse and fine levels in 2D. Missing information has to be reconstructed by interpolation and transformation.

where the available PPDFs are shown in Fig. 2(a) and the missing PPDFs, propagated from the other overlay level, are shown in Fig. 2(b). The macroscopic variables can simply be recovered by tri-linear interpolation. For the reconstruction of the missing PPDFs a transformation step is required. To keep the viscosity ν constant across the interface, the relaxation time τ has to be adapted. The relaxation time τ_f on the fine level f is obtained from the coarse level c by

$$\tau_f = m\left(\tau_c - \frac{1}{2}\right) + \frac{1}{2}, \tag{12}$$

where $m = \delta x_c / \delta x_f$ defines the refinement ratio. According to [25], incoming PPDFs are split into their equilibrium and non-equilibrium parts

$$f_i^{in} = f_i^{eq} + f_i^{neq}. \tag{13}$$

The non-equilibrium part of the PPDFs can be expressed by

$$f_i^{neq} = -\frac{\delta t \tau}{c_s^2} t_i Q_{i\alpha\beta} \partial_\alpha \rho u_\beta = \delta t \tau C(\rho, u), \tag{14}$$

where $Q_{i\alpha\beta} = \xi_{i\alpha}\xi_{i\beta} - c_s^2 \delta_{\alpha\beta}$ is summed over equal indices. In this equation $\delta t \tau$ defines the grid dependence, while $C(\rho, u)$ is independent of the grid resolution. The relation $f_i^{neq,f} / f_i^{neq,c}$ can be written as

$$\frac{f_i^{neq,f}}{f_i^{neq,c}} = \frac{\delta t_f \tau_f C(\rho, u)}{\delta t_c \tau_c C(\rho, u)} = \frac{1}{m}\frac{\tau_f}{\tau_c}, \tag{15}$$

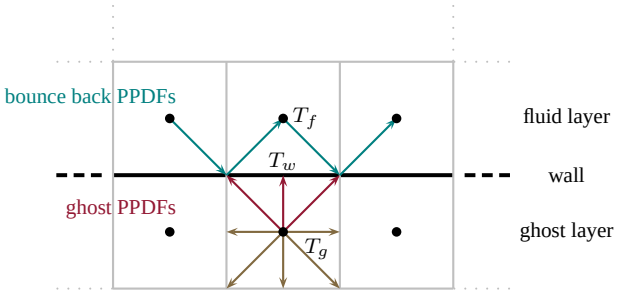

Figure 3 A ghost layer at the wall of the plate is required to provide incoming PPDFs g_i for the temperature of the fluid cells. A simple bounce back is performed for the PPDFs in the LBGK method.

and assuming $f_i^{eq} = f_i^{eq,c} = f_i^{eq,f}$, Eqs. 13 and 15 lead to

$$f_i^{in,f} = \tilde{f}_i^{eq} + \left(\tilde{f}_i^{in,c} - \tilde{f}_i^{eq}\right) \frac{1}{m} \frac{\tau_f}{\tau_c} \tag{16}$$

and

$$f_i^{in,c} = f_i^{eq} + \left(f_i^{in,f} - f_i^{eq}\right) m \frac{\tau_c}{\tau_f} \tag{17}$$

for the transformation from the coarse to the fine grid and vice versa. The functions $\tilde{f}_i$ in Eq. 16 are the PPDFs obtained by the interpolation step on the coarse grid. The same interpolation and transformation step is performed for the temperature T and the thermal PPDFs g_i.

Boundary Conditions

As for the imposed boundary conditions for nasal cavity flows a *Dirichlet condition* is used for the velocity and the temperature at the inflow region. A parabolic velocity profile, which is formulated as a function of the distance to the wall, is used to prescribe a certain volume flux, while for a constant inflow temperature of 20°C the equilibrium distribution functions are calculated at every boundary cell. Here, the density is extrapolated in surface normal direction using a *von Neumann condition*. The no-slip wall-boundary condition uses the interpolation method for inclined walls proposed by Bouzidi et al. [26]. The temperature is set to a constant value of 37°C body temperature at the wall. The outflow boundary condition is based on the formulation by Finck et al. [12] and imposes a constant pressure distribution.

For the simulation of the flow over a heated isothermal flat plate a *Dirichlet condition* is used at the inflow, prescribing a Blasius profile [27]. In addition, a *von Neumann condition* is prescribed for the density ρ. The temperature T_{in} at the inlet is set to

$$T_{in}(x,z) = T_w - \left| \frac{T_\infty f'(\eta)}{\frac{1}{2}\sqrt{\frac{\kappa T_\infty}{x}} \cdot (\eta f'(\eta) - f(\eta))} \right|, \tag{18}$$

where $\eta = z\sqrt{u_\infty/(\nu x)}$ is the so-called similarity parameter at coordinate (x, z) and $f(\eta)$ is the similarity stream function. The outflow condition is based on the formulation in [12] and imposes a constant density and a *von Neumann*

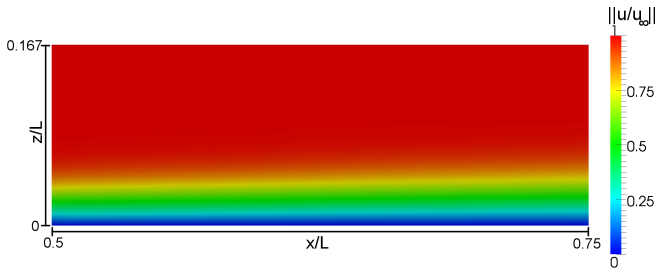

(a) velocity boundary layer

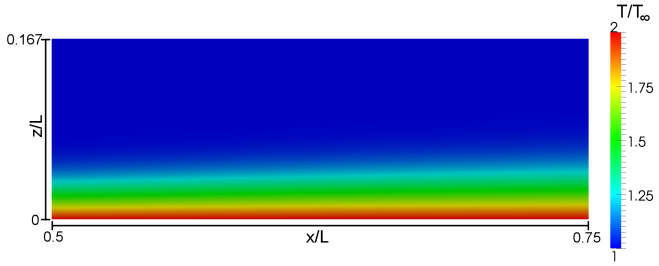

(b) temperature boundary layer

Figure 4 Velocity and temperature profile over an isothermal heated flat plate at $Re_L = 10^4$ and $Pr = 1.0$. At the inflow (left) a Blasius profile is prescribed.

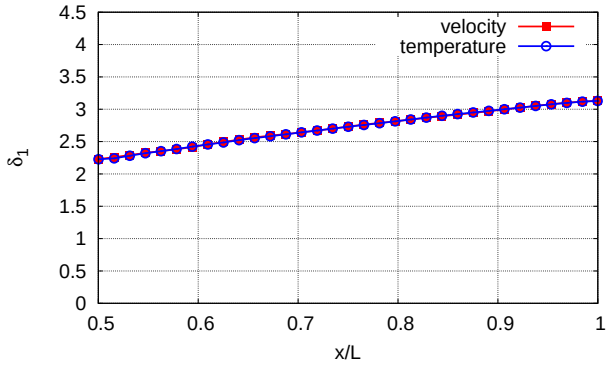

Figure 5 Boundary-layer displacement thickness δ_1 of the velocity and temperature.

condition for the velocity components and for the temperature. A no-slip wall condition is used for the flat plate performing a bounce-back of the PPDFs at the cell surfaces [28]. To set a constant temperature on the surface of the plate a ghost layer outside the fluid domain is introduced. To define the temperature T_w on the wall, the temperature T_g in the ghost layer cells is required to be

$$T_g = 2T_w - T_f, \tag{19}$$

where T_f is the temperature in the according fluid cell (see Fig. 3). Then, the PPDFs in the ghost cells are replaced by their temperature dependent equilibrium distribution functions, so that all required incoming PPDFs in the fluid cells are available and a heat transfer from the plate to the fluid is accomplished. In spanwise direction a periodic boundary condition, connecting cells in the positive and negative $y-$direction, is set.

Table 2 Structural features of the nasal cavity geometry and computational setup for flow simulations with the LBM with a volume flux of 125 ml/sec per averaged nostril. The locations 'left' and 'right' correspond to the patient's point of view.

Group	*category*	*structural features*	Re	Pr	$\bar{u}_{in}/\xi_0$	*Blocks*	*Cells*
N_{poor}	poor	- small hydraulic diameter of pharynx - missing inferior turb. in right cavity - missing center turbinate in left cavity - broad orifice to left paranasal sinus - hole in septum - notch in pharynx area	710	0.72	0.0058	56	47.4×10^6

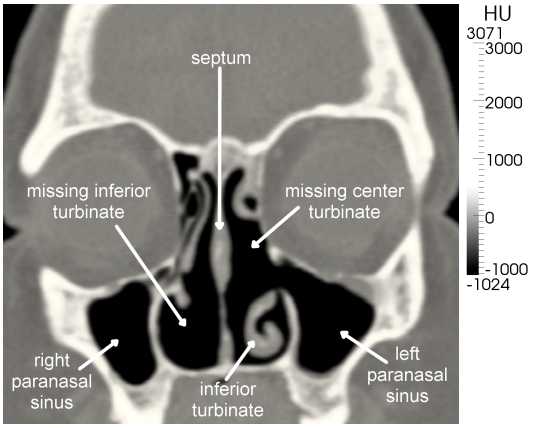

(a) Frontal slice of the CT image used for the extraction of the nasal cavity surface (see Fig. 6(b)).

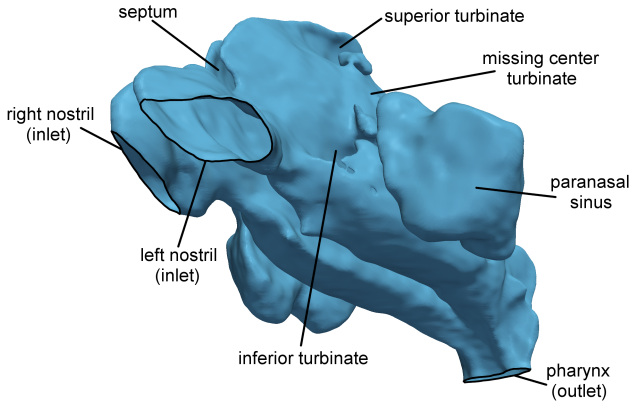

(b) Surface of the nasal cavity N_{poor} (see Tab. 2) extracted from the CT volume image shown in Fig. 6(a) with an in-house extraction tool.

Figure 6 CT image of the human nasal cavity and the according extracted surface. LBM-simulations are carried out for the inspiration process, i.e., the inflow condition is set at the nostrils and the outflow condition at the pharynx.

Grid Generation

The computational grid is created by an automatic *Cartesian grid* generator. For this purpose, the surface of the nasal cavity is extracted with an in-house segmentation tool from *Computer Tomography (CT)* images. A *Seeded Region Growing* algorithm [29] is used to identify the volume of the nasal cavity by placing seed points inside the fluid domain and recursively evaluating the neighborhood depending on a threshold range. The surface is then extracted using the *Marching Cubes* algorithm [30] and smoothed using a *Windowed Sinc Function* [31] removing high wavenumbers of the surface curvature. An initial bounding box is fit around the geometry, which is given in *stereolythography (STL)* format. Then, this box is continuously split into eight smaller boxes until a user-defined refinement-level ς is reached. Cells outside the geometry are removed during this process. This yields a grid distance of $\delta x = l_0/2^{\varsigma_{max}}$, where l_0 is the edge length of the initial boundary box on level $\varsigma = 0$ and ς_{max} is the maximal refinement level.

To obtain a multi-level grid, a level bandwidth b in addition to the maximal and minimal refinement level ς_{min} and ς_{max} is defined. The bandwidth defines the distance from the wall, which contains cells on the finest level ς_{max}. According to b, cells outside this bandwidth are only refined to ς_{min}. A smoothing step is required to guarantee that the level distance $\Delta\varsigma$ between a cell c and its neighbor $N_i(c)$ in the i-direction is less or equal 1

$$\Delta\varsigma(N_i(c)) = \varsigma(c) - \varsigma(N_i(c)) \leq 1. \tag{20}$$

To avoid $\Delta\varsigma(N_i(c)) > 1$, cells on the coarser level are refined to meet the requirements. For parallelization, the grid is either split by a *Hilbert decompositioning* method using space filling curves as described by Sagan in [32] or by the graph partitioning tool METIS based on the work in [33].

Results

Flat-plate Flow

To evaluate the LBGK and TLBGK method, the simulation of a three-dimensional flow over an isothermal heated flat plate is performed at a REYNOLDS number of $Re_L = 10^4$ based on the freestream velocity u_∞ and the length of the plate L and a PRANDTL number of $Pr = 1.0$. A Blasius profile is prescribed at $0.5x/L$. The computational grid consists of 0.7×10^6 cells and has a cell resolution of $\Delta x/L = 4.88 \times 10^{-3}$, where Δx is the grid distance. In the spanwise direction the fluid domain consists of 4 cells, where for the boundary cells a periodic condition is applied. Fig. 4(a) and Fig. 4(b) show the boundary layer for the velocities and the temperature, respectively. Except

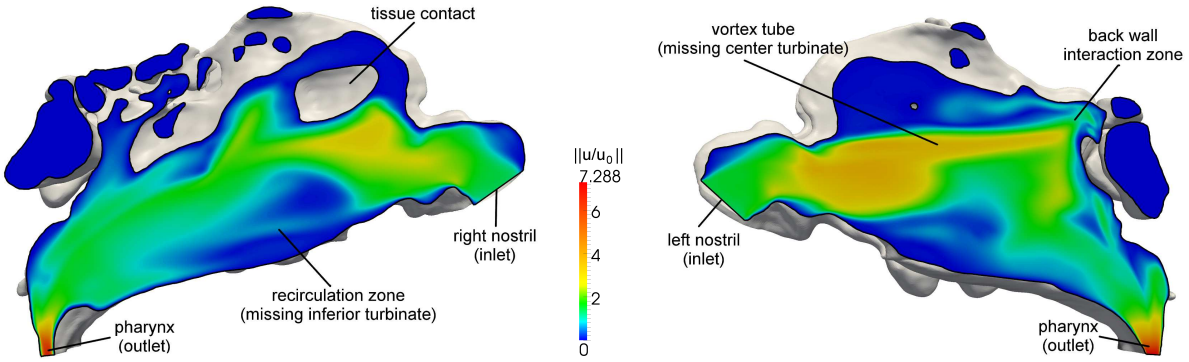

(a) velocity distribution in the right and left nasal cavity

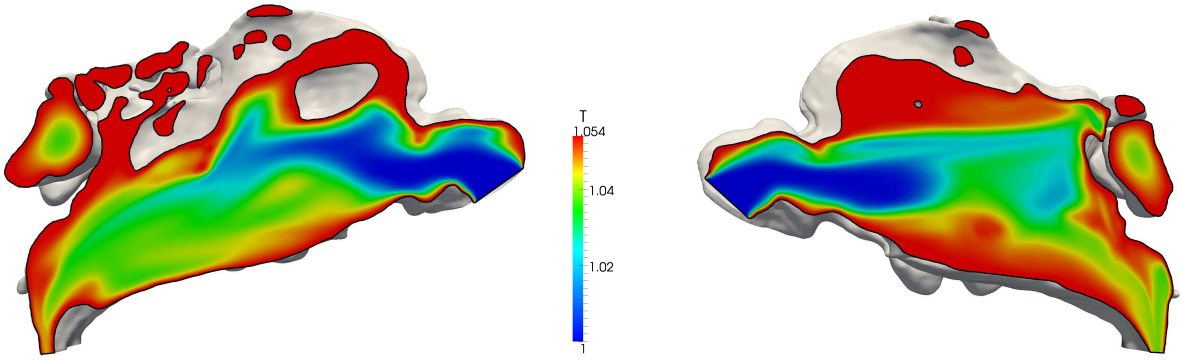

(b) temperature distribution in the right and left nasal cavity

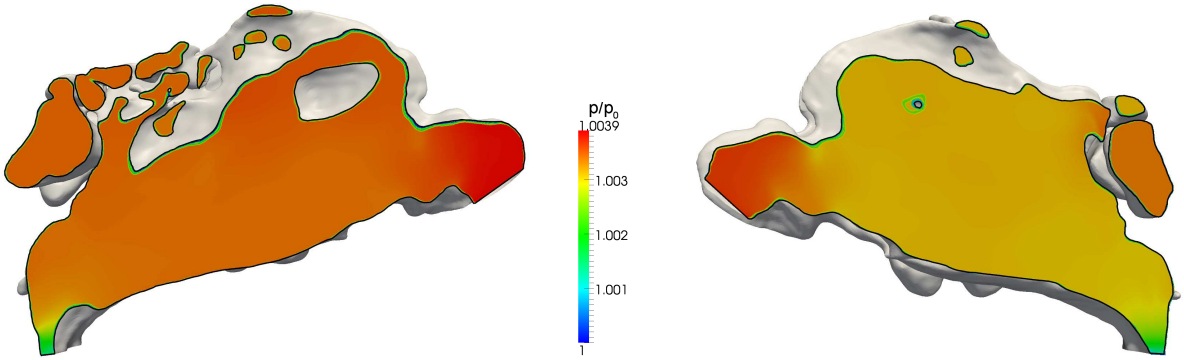

(c) static pressure distribution in the right and left nasal cavity

Figure 7 Velocity, temperature and static pressure distribution in the right and left nasal cavity.

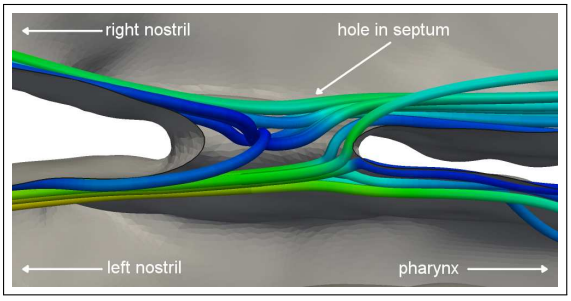

(a) the flow passes a hole in the septum from the left to the right nasal cavity

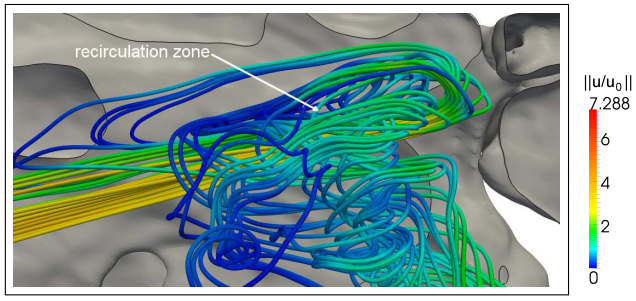

(b) reversed flow caused by a vortex system located close to the back wall in the left nasal cavity

Figure 8 Streamlines in the region of the hole in the septum and the region of the back wall, where the flow interacts with the wall and creates reversed flow zones and streamwise vortices.

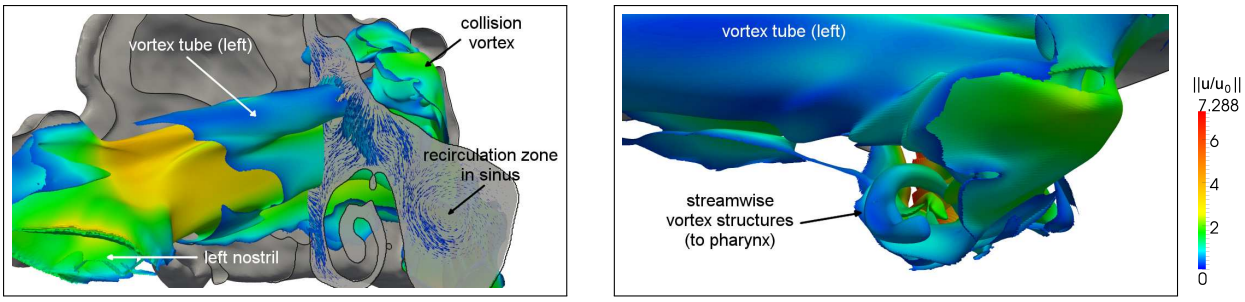

(a) side view on the vortex tube in the left nasal cavity; in the back the collision vortex according to Fig. 8(b) can be seen

(b) top view onto streamwise vortices forming a vortex pair; a part of the vortex tube shown in Fig. 9(a) can be seen

Figure 9 Vorticity contours in the left nasal cavity. A major vortex tube interacts with the back wall of the cavity and creates a reversed flow zone and streamwise vortices.

for the color inversion, the boundary-layer thicknesses are identical. The temperature of the plate T_w was set to twice the inflow temperature T_∞. As depicted in Fig. 5 the displacement thickness for the velocity

$$\delta_1^u = \int_0^\infty \left(1 - \frac{u(z)}{u_\infty}\right) dz \tag{21}$$

and for the temperature

$$\delta_1^T = \int_0^\infty \left(1 - \frac{T_w - T(z)}{T_\infty}\right) dz \tag{22}$$

collapse. This reflects, that the heat diffusion coefficient κ is equal to the viscosity ν at a PRANDTL number of $Pr = 1.0$, which also leads to the equality of Ω in Eq. 1 and Ω_T in Eq. 9.

Nasal-cavity Flow

Investigations of the flow and temperature field were carried out for a nasal cavity N_{poor} shown in Fig. 6(b). This nasal cavity was previously categorized as poor concerning its functionality, which is based on pressure loss measurements with a rhinomanometry method by rhinologists and the subjective evaluation by the patient. Tab. 2 lists the structural features of the geometry. Comparing the hydraulic diameters of the nostrils and the hydraulic diameter of the pharynx shows that the surface area of the pharynx is much smaller than those of the nostrils. This patient has a missing center turbinate on the left side and a missing inferior turbinate on the right side, which were removed in a rhino-anaplasty. In the region of the missing turbinate on the left side a big orifice exists to the left paranasal sinus. Additionally, this patient suffers from a hole in the septum and has a notch in the pharynx area. Based on the extracted surface in Fig. 6(b) a Cartesian mesh is automatically created, containing 47.4×10^6 cells of the same level with a cell edge length of 0.11mm. For parallelization the grid is split into 56 blocks with the graph partitioning tool METIS [33]. The REYNOLDS number $Re = D_h \cdot (\bar{u}_{in}/\xi_0)/\nu = 710$ is based on the kinematic viscosity ν, the mean hydraulic diameter of the nostrils D_h and a dimensionless mean inflow velocity $\bar{u}_{in}/\xi_0 = 0.0058$ obtained from a mean volume flux of 125ml/sec per nostril. The inflow temperature is set to 20°C and the surface temperature to 37°C body temperature. A PRANDTL number of $Pr = 0.72$ is used.

Considering the sideways directed inlet planes at the nostrils as depicted in Fig. 6(b) the flow is accelerated towards the inner wall of the nasal cavity on both sides. On the left side the fluid is accelerated due to a contraction of the passage near the nostril and forms a vortex tube (see Fig. 9(a)). Due to the missing center turbinate the fluid is transported towards the back and interacts with the wall. As shown in Fig. 8(b) and Fig. 9(b) this causes the formation of a recirculation area. Fig. 8(a) illustrates a top view on the region of the hole in the septum and evidences that for inspiration the fluid is transported from the left to the right nasal cavity by passing this orifice. Only a slowly rotating vortex appears in the left paranasal sinus although the opening is extremely widened due to the missing center turbinate (see Fig. 9(a)). In the right nasal cavity, the fluid is accelerated towards a tissue contact as depicted in Fig. 9(a) on the left side. This contact inhibits the fluid to flow along the upper region to the olfactory organ. In the region of the missing lower turbinate a recirculation zone is formed. This is shown in Fig. 7(a) on the left side, where an area of slowly moving fluid can be identified. Due to the small hydraulic diameter of the pharynx in contrast to the hydraulic diameters of the nostrils the fluid is accelerated on both sides in the bifurcation region of the left and right cavity (see pharynx region in Fig. 7(a), both cases).

The breathing capability is evaluated by considering the dimensionless pressure loss $\Delta p/p_0 = (p_{in} - p_{out})/p_0$ from the nostrils to the pharynx, where p_0 is the reference pressure. The influence of the dynamic pressure is rather low and therefore only the static pressure is considered. Fig. 7(c) shows the pressure distribution in the left and right nasal cavity of N_{poor}. In the left cavity the major pressure loss is caused by the narrowing of the channel close to the left nostril. Only small gradients can be observed in the region of the missing turbinate. A stronger gradient is shown close to the pharynx in the bifurcation zone, where the diameter of the passage is reduced. A similar observation can be made for the right nasal cavity.

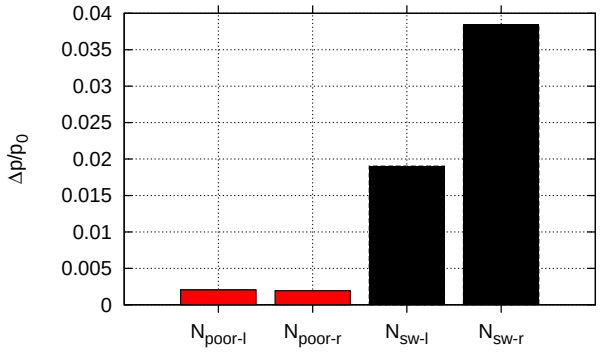

Figure 10 Comparison of the static pressure loss $\Delta p/p_0$ of the nasal cavity N_{poor} and a swollen nasal cavity N_{sw}. The indices 'l' and 'r' constitute the left and right cavity, respectively.

A comparison with the results for a swollen nasal cavity geometry N_{sw} in Fig. 10 reveals that the pressure loss in both cavities is only small for N_{poor}. Breathing problems reported by the patient are in this case probably only caused by the formation of recirculation areas and zones of reversed flow.

To evaluate the heating capability of the nasal cavity, the mean temperature increase $\Delta\bar{T} = \bar{T}_{out} - \bar{T}_{in}$ from the nostrils to the pharynx is determined and compared to results obtained for a nasal cavity not suffering from surgically removed nasal structures (geometry N_{ns}), i.e., the center turbinate in the right cavity and the inferior turbinate in the left cavity are still present (compare Tab. 2). As shown in Tab. 3 the air is heated by $\Delta\bar{T}_{poor} = 10.33°\text{C}$ in the nasal cavity N_{poor}, while in N_{ns} the temperature increase is $\Delta\bar{T}_{ns} = 15.49°\text{C}$. This reflects a reduced heating capability of the nasal cavity N_{poor}. Although the heating efficency increases with an increase of the surface area A (see Tab. 3), they do not necessarily correlate in general. The geometry of the nasal cavity not only contains the turbinate passages, but also the paranasal and the forehead sinuses, which account for a large increase of the surface area. However, most of the fluid is transported through the turbinate passages, while the paranasal and forehead sinuses are only connected to the main surface by small orifices. Consequently, they have only a minor effect on the flow and only account for a small amount of the temperature increase during inhalation. This can exemplarily be seen in Fig. 9(a), where the velocity magnitude in the right nasal cavity is plotted with vectors on a plane cutting the left paranasal sinus. Only a slowly turning vortex appears in this region, although the orifice to the sinus is enhanced due to the missing center turbinate.

The presented procedure of analysis, based on the evaluation of evolving flow structures, the pressure loss and the heating capability, leads to a fundamental understanding of the flow in the human nasal cavity and of the influences of the geometry on its functionalities. The efficient parallel LBM and TLBM algorithm to simulate the flow and temperature field, combined with a fast and easy grid generation makes this procedure a valuable tool for the simulation and analysis of flows in intricate geometries.

Table 3 Comparison between the mean temperature increase $\Delta\bar{T} = \bar{T}_{out} - \bar{T}_{in}$ and the surface area A of the nasal cavity N_{poor} and a nasal cavity N_{ns}.

	$A(cm^2)$	$\bar{T}_{in}(°C)$	$\bar{T}_{out}(°C)$	$\Delta\bar{T}(°C)$
N_{poor}	275.45	20	30.33	10.33
N_{ns}	373.32	20	35.49	15.49

The calculations were performed on a Nehalem-based cluster at HLRS Stuttgart with a CPU clocking of 2.8GHz on 56 cores. A solution convergence with a mean residual of 10^{-8} was reached after approx. 48 hours of computation time and 2.0×10^5 iterations.

Conclusions

A method to analyze the breathing and heating capability of human nasal cavities was presented in this paper. An in-house segmentation tool allows the extraction of the surface of the nasal cavity from CT-data. A fast and easy grid generation process automatically creates a computational mesh from the surface to be used in simulating the velocity, temperature and pressure distribution in the nasal cavity for inspiration. A Lattice-Boltzmann and a Thermal Lattice-Boltzmann Method is used to numerically solve the governing equation of the flow problem.

The simulation of laminar thermal and velocity boundary layers over a heated isothermal flat plate shows that the streamwise development of the displacement thickness for both cases collapse for a PRANDTL number of $Pr = 1.0$ indicating the correctness of the TLBM. Due to the simplicity and ease of parallelization of the algorithm, flow simulations can be performed efficiently on large scale compute clusters.

A preliminary dissection of the geometry of the nasal cavity in cooperation with rhinologists and the subjective evaluation of the patient reveal anatomical anomalies and potential reasons for an impaired breathing and heating capability. The breathing capability is evaluated by considering the pressure distribution, the pressure loss from the nostrils to the pharynx, the formation of recirculation and reversed flow zones, and their impact on the flow behavior. The heating capability is investigated by considering the mean temperature increase from the nostrils to the pharynx and comparing the results to a healthy nasal cavity. The analysis was exemplarily performed for two nasal cavities, one with surgically removed turbinates and the other with swollen turbinates. As expected, the pressure loss of the nasal cavity with swollen turbinates is higher than that for the nasal cavity with removed turbinates. However, the formation of recirculation and reversed flow zones reduce the breathing capability in the modified cavity by directing the fluid in the upstream direction and increasing the

arclength of particle paths. An analysis of the temperature distribution showed that the nasal cavity deformed by rhino-anaplasty has a considerably reduced heating capability compared to a cavity not suffering from such modifications. The mean temperature increase in the nasal cavity after rhino-anaplasty is $10.33°$C while the nasal cavity with intact anatomical structures increases the temperature by $15.49°$C. The surface area of the nasal cavity does not necessarily correlate with the heating capability, since most of the fluid is transported through the turbinate passages and paranasal and forehead sinuses only have a minor effect on the temperature increase. The results reveal, that for an a-priori evaluation of the nasal cavity functions, the analysis of the flow and temperature field can reproduce the properties of the nasal cavity in agreement with the patients observations, such that the here presented method seems to be applicable in the process of surgical intervention planning.

Further simulations of the flow in pre- and post-surgical nasal cavities will give insight to standardized surgical interventions. To understand the effect of the area of the nasal cavity surface on the heating capability, further investigations are required to find a correlation between these parameters. In addition, a coupling of the geometries of the nasal cavity, the pharynx, the larynx and the lung system will lead to an understanding of the complete respiratory system. In this case, inflow temperature variations to lower temperatures will give more insight into the protective function of the nasal cavity in winter. Particle transport algorithms based on these simulations will lead to an understanding of aerosol sedimentation in the lungs, e.g., the sedimentation of diesel aerosols in the bronchus causing cancer.

Acknowledgments

The research has been conducted under research grant WE-2186/5. The financial support by the German Research foundation (DFG) is gratefully acknowledged.

References

[1] L. Adams, W. Krybus, D. Meyer-Ebrecht, R. Rüger, J.M. Gilsbach, R. Mösges, and G. Schlöndorff. Computer-Assisted Surgery. *IEEE Computer Graphics and Applications*, 10(3):43–51, 1990.

[2] C. Brücker and K.I. Park. Experimental study of velocity fields in a model of human nasal cavity by DPIV. In *International Symposium on Turbulence and Shear Flow Phenomena*, pages 831–842, Santa Barbara, CA, USA, 1999.

[3] H. Masing. Experimentelle Untersuchungen über die Strömung im Nasenmodell. *European Archives of Oto-Rhino-Laryngology*, 189(1):59–70, 1967.

[4] R. Opitz and W. Limberg. Experimentelle Untersuchungen der Strömungen in einem Nasenmodell. *Abhandlungen aus dem Aeorodynamischen Institut*, 32:120–129, 1996.

[5] R. Opitz and W. Limberg. Druckverlustmessungen an einem Nasenmodell bei unterschiedlichen Volumenströmen. *Abhandlungen aus dem Aeorodynamischen Institut*, 33:119–125, 1998.

[6] I. Hörschler, M. Meinke, and W. Schröder. Numerical simulation of the flow field in a model of the nasal cavity. *Computers & Fluids*, 32(1):39–45, January 2003.

[7] I. Hörschler, W. Schröder, and M. Meinke. Numerical Analysis of the Impact of the Nose Geometry on the Flow Structure. Part I: Septum Spurs. *Computational Fluid Dynamics JOURNAL*, 16(2):219–234, 2008.

[8] I. Hörschler, W. Schröder, and M. Meinke. Numerical Analysis of the Impact of the Nose Geometry on the Flow Structure. Part II: Nasal Valve and Lower Turbinate. *Computational Fluid Dynamics JOURNAL*, 16(3):243–260, 2008.

[9] I. Hörschler, W. Schröder, and M. Meinke. On the assumption of steadiness of nasal cavity flow. *Journal of Biomechanics*, 43(6):1081–1085, 2010.

[10] R.K. Freitas and W. Schröder. Numerical investigation of the three-dimensional flow in a human lung model. *Journal of Biomechanics*, 41(11):2446–2457, August 2008.

[11] G. Eitel, T. Soodt, and W. Schröder. Investigation of pulsatile flow in the upper human airways. *International Journal of Design & Nature and Ecodynamics*, 5(4):335–353, 2010.

[12] M. Finck, D. Hänel, and I. Wlokas. Simulation of nasal flow by lattice Boltzmann methods. *Computers in biology and medicine*, 37(6):739–749, June 2007.

[13] G. Eitel, R.K. Freitas, A. Lintermann, M. Meinke, and W. Schröder. Numerical Simulation of Nasal Cavity Flow Based on a Lattice-Boltzmann Method. In A. Dillmann, G. Heller, M. Klaas, H.-P. Kreplin, W. Nitsche, and W. Schröder, editors, *New Results in Numerical and Experimental Fluid Mechanics VII*, volume 112 of *Notes on Numerical Fluid Mechanics and Multidisciplinary Design*, pages 513–520. Springer Berlin / Heidelberg, 2010.

[14] F. Alexander, S. Chen, and J.D. Sterling. Lattice Boltzmann thermohydrodynamics. *Physical Review E*, 47(4):R2249–R2252, April 1993.

[15] Y.H. Qian. Simulating thermohydrodynamics with lattice BGK models. *Journal of Scientific Computing*, 8(3):231–242, September 1993.

[16] Y. Chen, H. Ohashi, and M. Akiyama. Thermal lattice Bhatnagar-Gross-Krook model without nonlinear deviations in macrodynamic equations. *Physical Review E*, 50(4):2776–2783, October 1994.

[17] A. Bartoloni, C. Battista, S. Cabasino, P.S. Paolucci, J. Pech, R. Sarno, G.M. Todesco, M. Torelli, W. Tross, P. Vincini, R. Benzi, N. Cabibbo, F. Massaioli, and R. Tripiccione. LBE Simulations of Rayleigh-Benard Convection on the APE100 Parallel Processor. *Int. J. Mod. Phys. C*, 4:993–1006, 1993.

[18] Z. Guo, B. Shi, and C. Zheng. A coupled lattice BGK model for the Boussinesq equations. *International*

Journal for Numerical Methods in Fluids, 39(4):325–342, June 2002.

[19] P. L. Bhatnagar, E. P. Gross, and M. Krook. A Model for Collision Processes in Gases. I. Small Amplitude Processes in Charged and Neutral One-Component Systems. *Phys. Rev.*, 94(3):511–525, 1954.

[20] Y.H. Qian, D. D'Humières, and P. Lallemand. Lattice BGK Models for Navier-Stokes Equation. *Europhysics Letters (EPL)*, 17(6):479–484, February 1992.

[21] B. Lessani and M. Papalexandris. Time-accurate calculation of variable density flows with strong temperature gradients and combustion. *Journal of Computational Physics*, 212(1):218–246, February 2006.

[22] Y. Peng, C. Shu, and Y.T. Chew. A 3D incompressible thermal lattice Boltzmann model and its application to simulate natural convection in a cubic cavity. *Journal of Computational Physics*, 193(1):260–274, 2004.

[23] O. Filippova and D. Hänel. Boundary-Fitting and Local Grid Refinement for Lattice-BGK Models. *International Journal of Modern Physics C*, 9(8):1271–1279, 1998.

[24] A. Dupuis and B. Chopard. Theory and applications of an alternative lattice Boltzmann grid refinement algorithm. *Physical Review E*, 67(6):1–7, June 2003.

[25] B. Chopard and M. Droz. *Cellular Automata Modeling of Physical Systems*. Cambridge University Press, Cambridge, 1998.

[26] M. Bouzidi, M. Firdaouss, and P. Lallemand. Momentum transfer of a Boltzmann-lattice fluid with boundaries. *Physics of Fluids*, 13(11):3452–3459, 2001.

[27] H. Schlichting and K. Gersten. *Boundary-Layer Theory*. Springer, Berlin Heidelberg New York, 8th edition, 2000.

[28] D. Hänel. *Molekulare Gasdynamik, Einführung in die kinetische Theorie der Gase und Lattice-Boltzmann-Methoden*. Springer-Verlag, 2004.

[29] R. Adams and L. Bischof. Seeded Region Growing. *IEEE Transaction on Pattern Analysis and Machine Intelligence*, 16(6):641–647, 1994.

[30] W.E. Lorensen and H.E. Cline. Marching cubes: A high resolution 3D surface construction algorithm. *ACM SIGGRAPH Computer Graphics*, 21(4):163–169, 1987.

[31] G. Taubin, T. Zhang, and G. Golub. Optimal Surface Smoothing as Filter Design. *Computer Vision-ECCV96*, 20404:283–292, 1996.

[32] H. Sagan. *Space-Filling Curves*. Springer, 1st edition, 2007.

[33] G. Karypis and V. Kumar. A Fast and High Quality Multilevel Scheme for Partitioning Irregular Graphs. *SIAM Journal on Scientific Computing*, 20(1):359, 1998.